CHAPTER 2

BACKGROUND

2.1 General properties of ZnO

2.1.1 Crystal structure [33−34, 102−103]

ZnO is a II-VI compound semiconductor. Figure 2.1 shows the phase diagram of the Zn-O binary system. The condensed Zn-O system on equilibrium solid phase at 0.1 MPa hydrostatic pressure reveals the hexagonal closed packed (hcp) structure of ZnO with limited composition range (49.9 at% Zn and 50.0 at% O), and cubic structure of ZnO_2 with unknown composition range (~66.7 at% O). ZnO_2 can be possible due to the previous reports, but the conditions on the temperature and other natures for transforming to this structure are still unknown. In addition, ZnO in a face centered cubic (fcc) structure form can appear at elevated hydrostatic pressure due to its stability. It also has been reported that ZnO can exist metastable at room temperature in either of two cubic structures of sphalerite (e.g. ZnS) and rock salt (e.g. NaCl). Table 2.1 summarizes data related to Zn-O crystal structures.

The types of ZnO crystal structure, consisting of wurtzite (B4), zinc blende (B3) and rocksalt (or Rochelle salt) (B1), was shown in Figure 2.2.

Table 2.1 Zn-O crystal structure data [102]

	Stable phases at 0.1 MPa			Other phases	
	Zn	ZnO (I)	ZnO_2	ZnO (II) (a)	ZnO (III)
Composition, at% O	~0	49.9 to 50.0	~66.7	~50	~50
Pearson Symbol	*hP*2	*hP*4	*cP*12	*cF*8	*cF*8
Space Group	$P6_3/mmc$	$P6_3mc$	*Pa*3	$Fm\bar{3}m$	$F\bar{4}3m$
Prototype	Mg	ZnO (wurtzite)	FeS_2 (pyrite)	NaCl	ZnS (sphalerite)

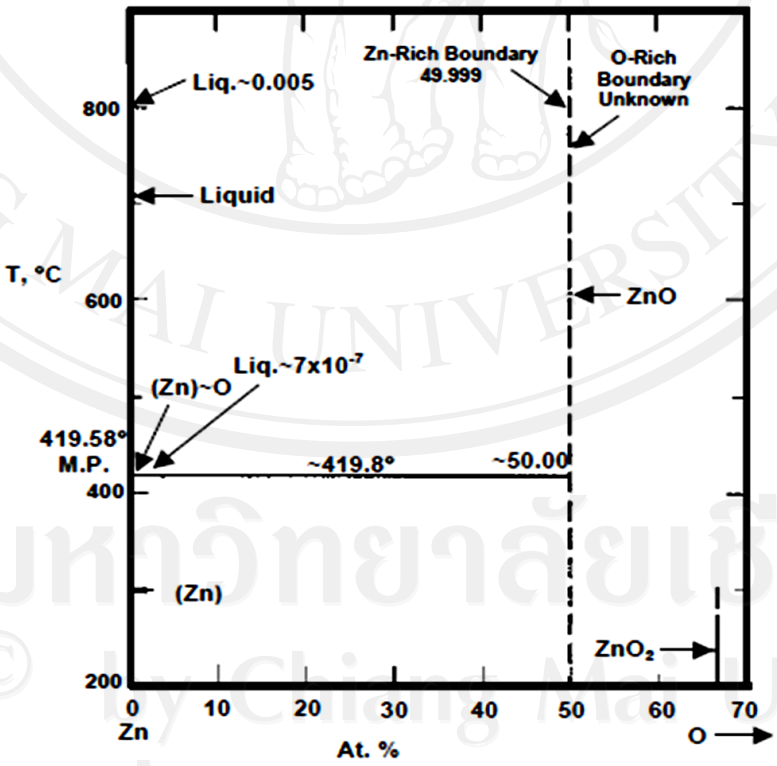

Figure 2.1 Phase diagram for condensed Zn-O system at 0.1 MPa [102]

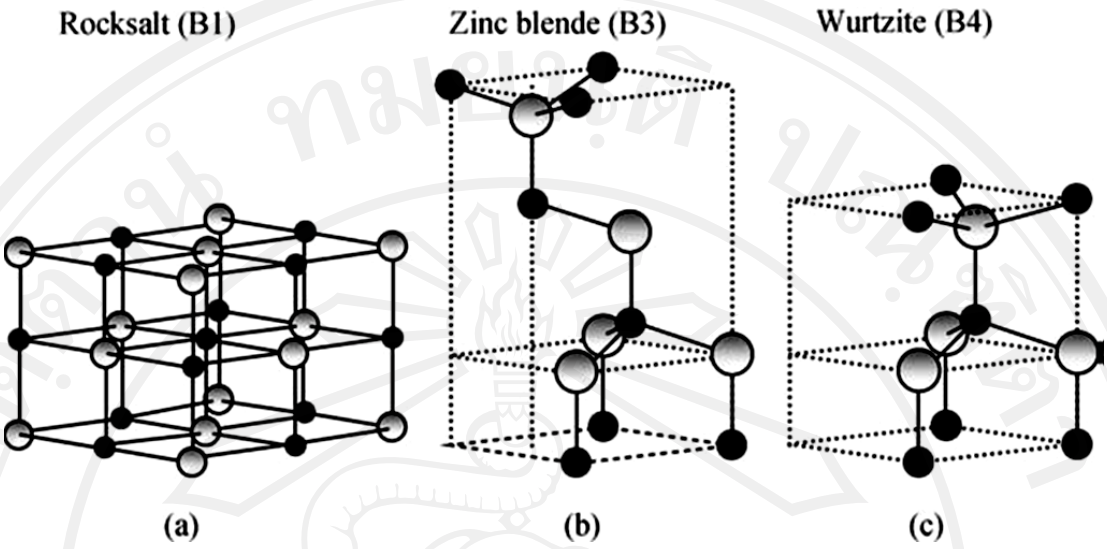

Figure 2.2 ZnO crystal structures: (a) cubic rocksalt (B1), (b) cubic zinc blende (B3) and (c) hexagonal wurtzite (B4) (Atoms in grey and black colors refer to Zn and O atoms, respectively [34].)

Commonly, ZnO is in wurtzite structure as shown in Figure 2.3. The wurtzite structure has a hexagonal unit cell with two lattice parameters a and c in the ratio of $c/a = \sqrt{8/3} = 1.633$ (in an ideal wurtzite structure) and belongs to the space group C_{6v}^4 in the Schoenflies notation and $P6_3mc$ in the Hermann-Mauguin notation (Table 2.1). This structure consists of the arrange of two-atom type sublattices in form of hexagonal close packed (hcp) interpenetration along with three fold *c*-axis by amount of $u = 3/8 = 0.375$ (in an ideal wurtzite structure) in fractional coordinates. The internal parameter u is defined as the length of the bond parallel to the *c*-axis (anion-cation bond length or the nearest-neighbor distance), namely the b parameter (0.375 in ideal crystal). The a parameter is identified as the edge length of the basal plan hexagon. The height of unit cell which is perpendicular to the basal plan is divided by

c parameter. α and β are bond angles (109.47° in ideal crystal), and $b_1^{'}$, $b_2^{'}$ and $b_3^{'}$ are the second-nearest-neighbor distances.

Inside a tetragonal unit cell, there are two-atom type sublattices with the arrangement shown that a group II atom is enclosed with four group VI atoms in tetrahedron shape, and on the contrary, a group VI atom is also enclosed with four group II atoms in tetrahedron. The crystallographic vectors of wurtzite are $\vec{a} = a\left(1/2, \sqrt{3}/2, 0\right)$, $\vec{b} = a(1/2, -\sqrt{3}/2, 0)$ and $\vec{c} = a(0, 0, c/a)$. In Cartesian coordinates, the basis atoms are $(0,0,0)$, $(0,0,uc)$, $a(1/2, \sqrt{3}/6, c/2a)$ and $a(1/2, \sqrt{3}/6, [u+1/2]c/a)$.

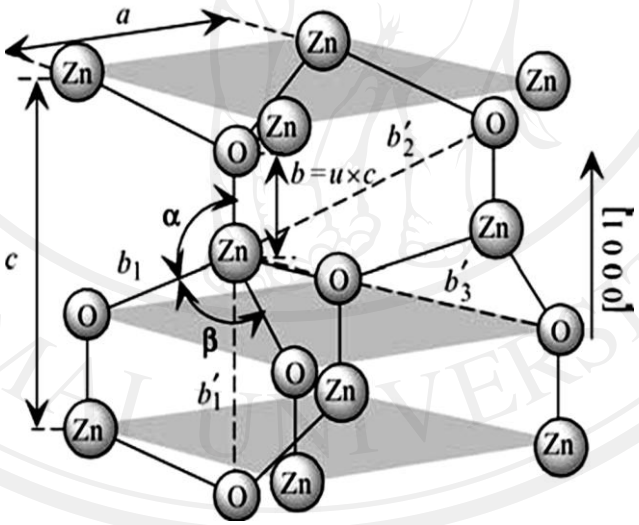

Figure 2.3 Schematic structure of wurtzite ZnO [34]

ZnO crystal under real situation, the wurtzite structure can shift from the ideal arrangement by varying the c/a ratio or the u value. The experimentally observed c/a ratios are smaller than ideal so it would lead to zinc blende phase. The relation between the c/a ratio and u parameter shown in Equation 2.1:

$$u = \left(\frac{1}{3}\right)\left(\frac{a^2}{c^2}\right) + \frac{1}{4}. \tag{2.1}$$

It is indicated that when the c/a ratio decreases, the u parameter increases. This is because a distortion of tetrahedral angles from long-range polar interaction.

The nearest-neighbor bond lengths along the *c*-direction, namely b and off *c*-axis, namely b_1 can be calculated as

$$b = cu \text{ and } b_1 = \sqrt{\frac{1}{3}a^2 + \left(\frac{1}{2} - u\right)^2 c^2}\,. \tag{2.2}$$

In addition to the nearest neighbors, there are three types of second-nearest neighbors designated as b'_1 (one along the *c*-direction), b'_2 (six of them) and b'_3 (three of them) with the bond lengths:

$$b'_1 = c(1-u),\ b'_2 = \sqrt{a^2 + (uc^2)} \text{ and } b'_3 = \sqrt{\frac{4}{3}a^2 + c^2\left(\frac{1}{2} - u\right)^2}\,. \tag{2.3}$$

The bond angles, a and b, are given by

$$\alpha = \pi/2 + across\left[\left(\sqrt{1 + 3(c/a)^2(-u + 1/2)^2}\right)^{-1}\right], \tag{2.4}$$

$$\beta = 2arcsin\left[\left(\sqrt{4/3 + 4(c/a)^2(-u + 1/2)^2}\right)^{-1}\right].$$

Usually, the lattice parameters are calculated by the Bragg law under X-ray diffraction (XRD) technique. Moreover, this technique is also used for determining the composition of compounds. In the case of epitaxial layers on foreign substrates,

strain and significant issues are included for analyzing them. The accuracy of X-ray diffraction and elastic parameter knowledge permit the determination of composition toward about 1% molar fraction. The parameter factors of the composition, including free charge, impurities, stress and temperature, also affect the determination of the lattice parameter. The difference of the electronegativities of the two elements correlates with c / a ratio so if the components have the high differences, it will show the large far from the ideal c / a ratio.

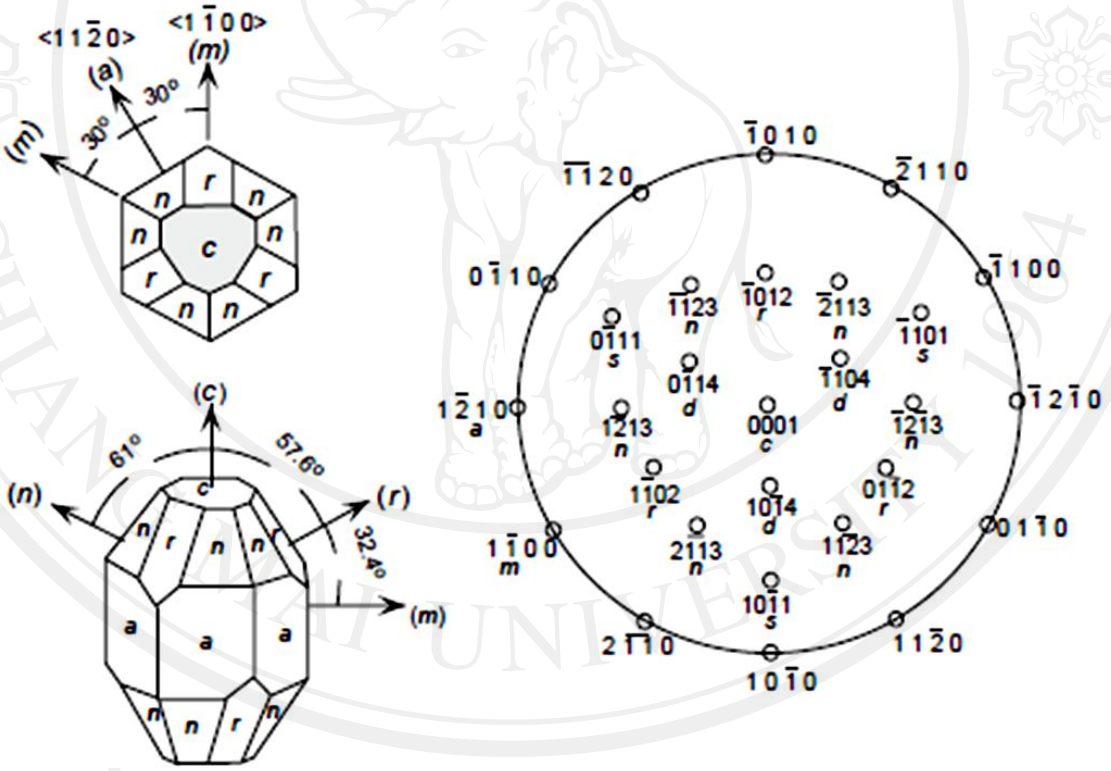

Common crystallographic planes in sapphire

Plane name	Miller index	*d* spacing
a	(11$\bar{2}$0)	2.379 Å
m	(10$\bar{1}$0)	1.375 Å
c	(0001)	2.165 Å
r	(1$\bar{1}$02)	1.740 Å
n	(11$\bar{2}$3)	1.147 Å
s	(10$\bar{1}$1)	1.961 Å

Angles between common planes

(0001) ^ (1$\bar{1}$02)	*c* ^ *r*	57° 35′
(0001) ^ (11$\bar{2}$3)	*c* ^ *n*	61° 11′
(0001) ^ (10$\bar{1}$1)	*c* ^ *s*	72° 23′
(0001) ^ (11$\bar{2}$1)	*c* ^	79° 37′
(0001) ^ (11$\bar{2}$0)	*c* ^ *a*	90° 00′
(0001) ^ (10$\bar{1}$0)	*c* ^ *m*	90° 00′
(11$\bar{2}$0) ^ (10$\bar{1}$0)	*c* ^ *m*	30° 00′

Figure 2.4 Labeling of planes in hexagonal symmetry (for sapphire) [34]

The nomenclature of various planes of hexagonal semiconductors in two- and three-dimensional versions was shown in Figures 2.4 and 2.5. Since wurtzite ZnO lacks an inversion plane perpendicular to the *c*-axis, surfaces have either a group II element (Zn, Cd or Mg) polarity (referred to as Zn polarity) with a designation of (0001) or $(000\bar{1})$ A plane or an O polarity with a designation of $(000\bar{1})$ or (0001) B plane. The difference between these two directions is essential due to polarization charge. The important surface and associate directions, consisting of (0001), $(11\bar{2}0)$ and $(1\bar{1}00)$, and $\langle 0001\rangle$, $\langle 11\bar{2}0\rangle$ and $\langle 1\bar{1}00\rangle$, respectively, as shown in Figure 2.6. The basal plane (0001) is the most commonly used surface for growth. The other two planes are also important because they represent the primary directions used in reflection high-energy electron diffraction (RHEED) observations in molecular beam epitaxy (MBE) growth. Figure 2.5 shows a magnified view of labeling of planes in hexagonal symmetry. The (*tuvw*) coordinate system represents w as the unit vector in the *c*-direction. The lines simply show the symmetry only. If the lines connecting m-points among each other and a-points among each other were to be interpreted as the projection of those planes on the c-plane, the roles would be switched in that the lines connecting the m-points would actually represent the a-planes and lines connecting the a-points would actually represent the m-planes, which are normal to the plane of the page.

Due to the motif of ZnO structure involving the orientation of Zn and O ions, this directly affects the especially typical properties of ZnO listed in Table 2.2.

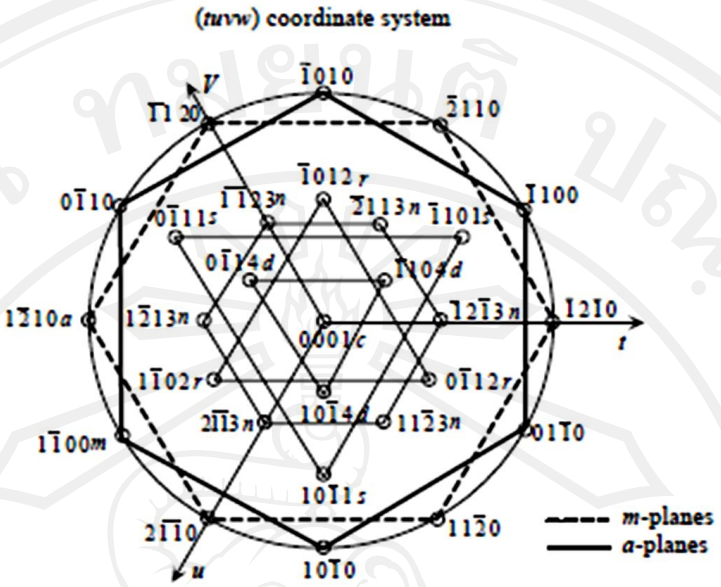

Figure 2.5 Labeling of planes in hexagonal symmetry in the $(tuvw)$ coordinate system [34]

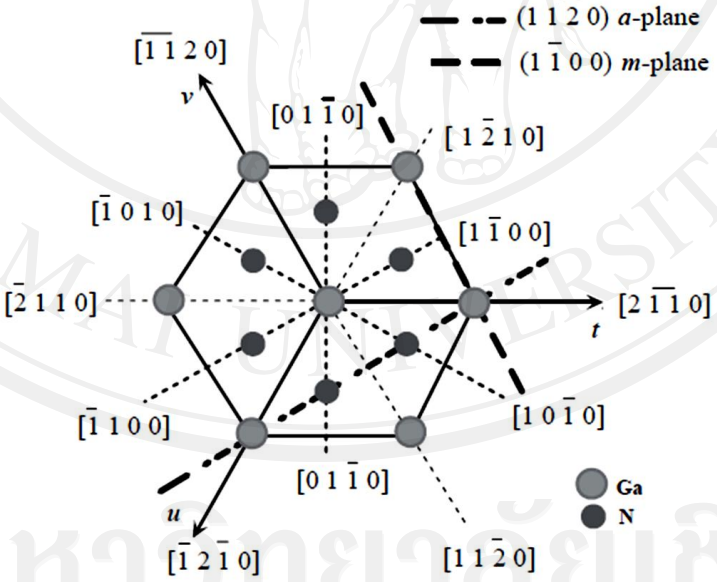

Figure 2.6 Orientations that are commonly used in wurtzite phase, namely, the $(11\bar{2}0)$ and $(1\bar{1}00)$ planes and associated directions are shown as projections on the (0001) basal plane [34].

Table 2.2 Properties of wurtzite ZnO [103]

Property	**Value**
Lattice parameters at 300 K:	
a_0	0.32495 nm
c_0	0.52069 nm
a_0 / c_0	1.602 (1.633 for ideal hexagonal structure)
u	0.345
Density	5.606 g/cm^3
Stable phase at 300 K	Wurtzite
Melting point	1975°C
Thermal conductivity	0.6, 1−1.2
Linear expansion coefficient (/°C)	a_0 : 6.5 x 10^{-6}, c_0 : 3.0 x 10^{-6}
Static dielectric constant	8.656
Refractive index	2.008, 2.029
Energy gap	3.4 eV (direct)
Intrinsic carrier concentration	<10^6 /cm^3
Exciton binding energy	60 meV
Electron effective mass	0.24
Electron Hall mobility at 300 K for low n-type conductivity	0.59
Hole effective mass	200 cm^2/V•s
Hole Hall mobility at 300 K for low p-type conductivity	5−50 cm^2/V•s

2.1.2 Electronic band structure [62, 104−106]

The band structure provides the electronic states of electron or hole. A complete understanding of the energy band structure of ZnO is important, in order to properly utilize the material in various device applications. X-ray or UV reflection/absorption or emission conventional techniques have been used to measure the electronic core levels in solids. Another important method for investigating the energy region is based on the photoelectric effect extending to the X-ray region, namely photoelectron spectroscopy (PES). Moreover, angle-resolved photoelectron spectroscopy (ARPES) technique built together with synchrotron radiation excitation have been well known as a powerful tool that can use for the experimental determination of bulk and surface electronic structures under the assumptions of k-conservation and single nearly free-electron like final band.

In worldwide case, ZnO direct bandgap semiconductor are the upmost valence band (VB) and the lowest conduction band (CB) at the same point in the Brillouin zone, namely at k = 0, i.e. at the Γ-point, so it is mainly interested in this region. The CB with symmetry Γ_7 including spin comes from the empty 4s levels of Zn^{2+} or the antibonding sp^3 hybrid states, adapting the views of ionic or covalent binding, respectively. The group-theoretical compatibility tables told Klingshirm that the bottom of the CB has Γ_1 symmetry without inclusion of spin and symmetry $\Gamma_1 \otimes \Gamma_7 = \Gamma_7$ with spin (Figure 2.7). The effective electron (more precisely polaron) mass is almost isotropic with a value around $m_e = (0.28 \pm 0.02) m_0$.

The VB, originating from the occupied 2p orbitals of O^{2-} or the binding sp^3 orbitals, are split without spin under the influence of the hexagonal crystal field into

two states, Γ_5 and Γ_1. Inclusion of spin gives a further splitting due to spin-orbit coupling into three two-fold-degenerate sub-VB of symmetries $(\Gamma_1 \oplus \Gamma_5) \otimes \Gamma_7 = \Gamma_7 \oplus \Gamma_9 \oplus \Gamma_7$, see Figure 2.7. These VB are labeled in all wurtzite-type semiconductors (like ZnS, CdS, CdSe or GaN) from higher to lower energies as A, B and C bands, or the heavy-hole, light-hole, and crystal field split-off bands, respectively. The most cases of the ordering of bands are $A\Gamma_9$, $B\Gamma_7$, $C\Gamma_7$ and the spin-orbit splitting is larger than the crystal field splitting. However, in ZnO case, the general consideration for a long time over whether the ordering of ZnO VB is $A\Gamma_9$, $B\Gamma_7$, $C\Gamma_7$ or $A\Gamma_7$, $B\Gamma_9$, $C\Gamma_7$ called "negative spin-orbit coupling" or inverted VB ordering. Actually, the spin-orbit coupling is always positive. The close-lying occupied Zn 4d levels plus the level repulsion may affect easily shift one Γ_7 level above the Γ_9 state resulting in the inverted VB ordering, which can directly discover toward the I^b-VII semiconductor CuCl. Due to the splitting of A and B valence bands upon the order of 5 meV as well as the selection rules (the transitions from the two upper $A\Gamma_9$ and $B\Gamma_7$ VBs to the Γ_7 CB band are dipole and spin flip allowed only for $E \perp \vec{c}$ and from the $C\Gamma_7$ VB only for $E \parallel \vec{c}$), as shown in Figure 2.7, the discussion about the symmetries of the A and B valence bands seem to be a storm in a tea cup.

The inverted VB ordering has been accepted by many authors since then [107]. In various references [108−110], the debates expose to the normal valence-band ordering in ZnO that it is still not convincing. Therefore, Klingshirn et al. [62] stand by the inverted VB-ordering with the reason that the majority of scientists has been affirmed it and use it throughout in the following. The effective hole masses in

ZnO are rather isotropic and similar to the A, B and C VBs with typical values of [111−119]

$$m_{h\perp,\parallel A,B} = 0.59m_0\,,\ m_{h\parallel C} = 0.31m_0\,, m_{h\perp C} = 0.55m_0\,. \tag{2.5}$$

Bands of symmetry Γ_7 may have a small k-linear term for $k \perp \vec{c}$ as indicated in Figure 2.7 for the A VB. This term can also occur for the C VB. On the contrary, for the CB, this effect is negligible.

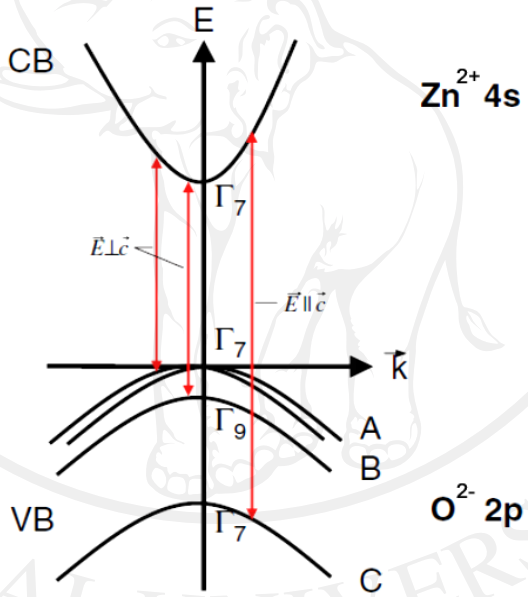

Figure 2.7 ZnO valence and conduction band structure diagram [105]

2.2 N-type doping of ZnO [34, 105, 120−121]

ZnO in a wurtzite structure is naturally an n-type semiconductor because of deviation from stoichiometry due to the presence of intrinsic defects such as O vacancies (V_O) and Zn interstitials (Zn_i). In other words, Look et al. [14] suggested that Zn_i rather than V_O is the dominant native shallow donor in ZnO.

Undoped ZnO shows n-type conductivity with electron densities of 10^{21} cm^{-3}. Unfortunately, that value has been reduced by MBE and hydrothermal methods, to about 10^{17} cm^{-3} and below 10^{14} cm^{-3}, respectively. However, by FSP, it has still unknown. The attainment of intentional n-type doping of ZnO is relatively easy compared to p-type doping. As n-type dopants, group III elements B, Al, Ga and In, and rare earth metals (group IIIB) Sc and Y can be used.

The group III elements, for example, Al, Ga and In, are shallow and efficient donors on Zn cation sites. A degenerate carrier gas is proved that it is because the Fermi energy is located in the band and in the bandgap shortly. This can described from Fermi-Dirac statistics. The limit between a description in terms of classical Boltzmann and degenerate Fermi-Dirac statistics is the so called effective density of states (n_{eff}), which is for ZnO at RT given by

$$n_{eff} = 2\left(\frac{2\pi m_e k_B T}{h^2}\right)^{3/2} = 4\times 10^{18} cm^{-3}. \qquad (2.6)$$

In fact, solutes, vacancies and interstitials can perturb the band structure, and introduce localized energy levels within the bandgap. A defect with energy level located near the conduction band may be able to donate an electron to the conduction band, namely, a donor. In defect chemical reactions, the ionization of donors and acceptors in ZnO can be written as

$$Sn(metal) = Sn_{Zn}^{\bullet} + e'' \ . \qquad (2.7)$$

The probability that a donor impurity at an energy level will be ionized given by Fermi statistics. If the ionization energy is of the same order as $k_B T$, then the

probability of ionization is high and the defect is known as a shallow donor. At room temperature (where k_BT = 0.025 eV) impurities with ionization energies of ≤0.05 eV are considered shallow. These shallow dopants will be effective at increasing the concentration of free electronic carriers. On the other hand, a deep donor refers to a solute with large ionization energy. At the interesting temperature, if the solute is not ionized it is essentially electrically inactive.

Moreover, Pearton et al. [120] revealed that there have been several explanations about doping in wide bandgap semiconductors. First, there can be compensation by native point defects or dopant atoms that locate on interstitial sites. Another one is the compensation with the substitutional impurity through the formation of a deep level trap. In some cases, strong lattice relaxations can drive the dopant energy level deeper within the gap. However, some systems may simply have a low solubility due to the chosen dopant limiting the accessible extrinsic carrier density. Substituted foreign atoms can also enhance the semiconducting properties of ZnO. In the presence of selected metallic vapors at elevated temperatures, the foreign metallic atom replaces a portion of the Zn atoms. The zinc atoms will be released from their lattice positions where they are vaporized and diffuse to crystal surface. This substitution process can strongly modify the crystal properties, depending upon the nature, concentration and valence of the foreign atoms. Specially, optical and electrical properties can be readily modified.

2.3 Flame spray pyrolysis [94, 122]

Flame spray pyrolysis (FSP) is one of the flame aerosol techniques for synthesizing nano-mixed oxides. In FSP process, the combustion of pressure-assisted

produced liquid spray droplets is self-sustaining, arising from the overall highly exothermic liquid precursor (metal precursor and solvent). One of the major advantages of FSP lies in the ability to utilize a broad range of liquid precursors including some inexpensive and non-volatile ones, however, the necessary first thing of self-sustaining flame is the usage selection limited with highly exothermic precursor. This critical effect, which is full of high enthalpy flame enough, will be discussed that it leads to dense nanoparticles with homogenous size distributions.

The particles formation by FSP can generally be categorized toward two possible routes: droplet-to-particle and gas-to-particle (see also Figure 2.8 for reference). In fact, in the most cases of FSP synthesis, spray droplets are evaporated to form metal vapor (gas) and then nucleates and grows to form fine particles (right hand side), while the formation under the droplet environment leads to hollow and/or larger particles.

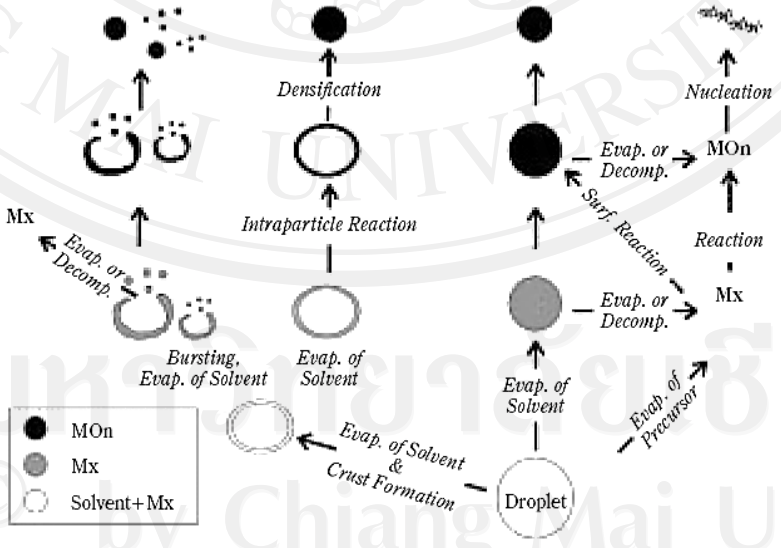

Figure 2.8 Various mechanisms for metal oxide formation by spraying dissolved metal precursors into a high-temperature reaction zone [122]

The formation of metal vapor requires sufficient combustion energy in the flame (>4.7 kJ/g_{gas}), or the decomposition/melting of the metal precursor before the evaporation of solvent ($T_{bp}/T_{d/mp}$< 1.05). The category of metal precursors, such as metal alkoxides, naphthenates, acetylacetonates and ethylhexanoates, is regularly selected for synthesizing nanoparticles via FSP, under gas-to-particle path. This path explained that the solvent is firstly evaporated leaving behind dried metal precursor to undergo solid state reactions and densification.

2.3.1 Particle growth and coagulation [90, 94]

Coagulation and sintering process are found after the formation of particles (either by gas-to-particle or droplet-to-particle) likes other general aerosol syntheses. The aerosol aggregation process can be easily described by particle evolution equations at high temperature. For particle coagulation, this process is given by the equation:

$$\frac{dN}{dt} = -\frac{1}{2}\beta N^2 \tag{2.8}$$

where N is the number concentration of particles and β is the collision frequency. From relating sintering effect, the loss of surface area (a) would have to be put into some parts of equation:

$$\frac{da}{dt} = \frac{1}{N}\frac{dN}{dt}a - \frac{1}{\tau}(a - a_s) \tag{2.9}$$

where the second term on the right hand of this equation for coalescence of an aggregate, which is driven by the characteristic sintering time for grain boundary

diffusion (τ) and difference between actual surface area and completely fused sphere surface area (a_s). In FSP synthesis of ZrO_2 particles, τ is given by:

$$\tau = 0.001703 \frac{RT\left(d_p / 2\right)^4}{w_b D_b(T) \gamma \Omega} \tag{2.10}$$

where R is the universal gas constant, T is the temperature, $w_b = 5 \times 10^{-10}$ m is the grain boundary width, $D_b(T)$ is the grain boundary diffusion coefficient for ZrO_2 as a function of temperature, γ is the surface tension, and Ω is the molar volume of diffusing species. From these equations, it is found that when higher flame temperature, metal concentration and residence time increase, the particle sizes increase from the effects of coagulation and sintering. In terms of the FSP operation, the flame temperature profiles and residence times can design by varying the ratio of liquid precursor feed flow rate to dispersant flow rate and also the overall enthalpy of liquid precursor. For the temperature profile as a function of the flame reaction process time, it was showed in Figure 2.9: titania was synthesized from $TiCl_4$ by oxidation in flame reactor [90]. For FSP process, the flame temperature can drop due to heat loss. Therefore, the particles in this step will not go through the sintering process because of the insufficient energy. Hence, only agglomeration between particles will take place in this case. Moreover, hard or soft agglomerates can be formed depending on the flame temperature in each zone. Hard agglomerates are a sintering formation over some part necking of particles. This is between the zone of full sintering and soft agglomerates. On the other hand, soft agglomerates are

reversible agglomerates held weakly by Van der Waals forces, formed at lower temperature a lot and without any form of sintering (fully or partly).

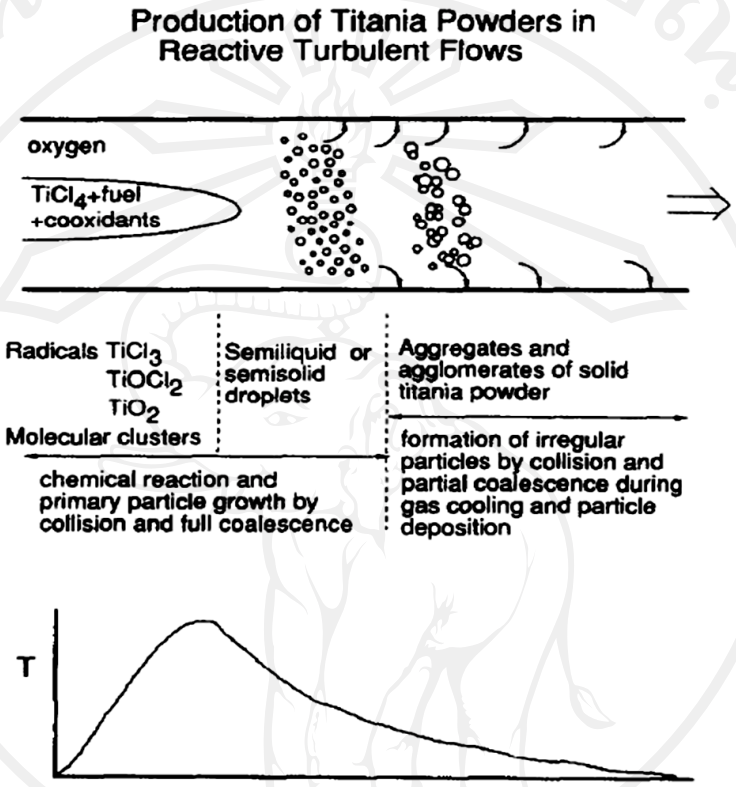

Figure 2.9 Schematic of titania synthesis by $TiCl_4$ oxidation by the "chloride" process [90]

2.4 Metal oxide for gas sensor [123−127]

To detect chemical species in the gas phase, the most suitable sensors of these types are semiconductor gas sensors using metal oxides. For differing of the gas sensing between other semiconductors and metal oxides, the first one undergoes irreversible chemical reactions for forming stable oxides upon exposure to air at high temperature while the last one remain stable from interacting with oxygen at their surfaces. Following gas sensing mechanism process, the possibilities of gas molecules

when they attach to samples are interact with (1) bulk grains, (2) electrode/oxide interface and (3) intergranular contacts. After that, the reactions on interface affect electron transferring within the metal oxide or a change in the resistance inside the metal oxide. The sensors can be divided into 3 groups under the electrical response from the physical origin:

a) bulk-conduction based sensor
b) metal/oxide (electrode/oxide) junction controlled sensor
c) surface-layer conductive (intergranular controlled) sensor

2.4.1 Surface conductive sensors [123]

This sensor type is justified that the gas species will be absorbed at the surface resulting in the chemical reactions around there, so this leads to the change in the conductance. These reactions, namely chemisorption, modify the surface of oxides, making the defect on surface layer to a depth of a few μm or less. Therefore, the operating temperature should be in low ranges enough to allow sufficient surface adsorption and to slow down the bulk defect equilibration processes. However, it should be high enough for catalysis reactions and charge transfer between the surface layer and the bulk interior. The working temperature of this sensor type is usually lower than that of the bulk conduction based gas sensors, typically 200–500°C, depending on the base oxide and the target application.

This thesis will mainly focus in this type of sensor from principles toward the practical applications.

2.4.1.1 Physical and chemical adsorption [123, 126]

The types of absorption of gas-phase atoms or molecules are (a) physisorption and (b) chemisorption. In the Lennard-Jones model, the energy of the system is represented as a function of adsorbate/adsorbent distance as shown in Figure 2.10. The lack of activation energy is due to this process using a Van der Waals dipole interaction only, so the rate of physisorption is not depending on temperature. However, the desorption of molecules requires an activation energy of ΔH_{PHY}. Hence, the rate of physisorption can be written as

$$d\Gamma_{PHY} / dt = k_{ads} P\left(\Gamma^0 - \Gamma\right) - k_{des}\Gamma\exp(-\Delta H_{PHY} / RT) \qquad (2.11)$$

where Γ^0, Γ, P and k are density of surface adsorption sites, density of sites covered by adsorbate, gas pressure and rate constants, respectively. The physisorption is mainly dominant at low temperature and minimal at high temperature because the second term (desorption) increases as temperature. At steady state, Equation 2.12 replaces with the Langmuir isotherm:

$$\theta = P / \left[P + \left(k_{des} / k_{ads}\right) exp\left(-\Delta H_{PHY} / RT\right)\right]. \qquad (2.12)$$

If the pressure is very low, it reduces to a sort of Henry's law expression

$$\theta \cong \left(k_{ads} / k_{des}\right) exp\left(\Delta H_{PHY} / RT\right) P \qquad (2.13)$$

where the fractional coverage, θ, varies directly proportional to the gas pressure.

On the other hand, a molecule can disengage into “atoms” upon the condition of dissociation energy (ΔE_D) much more. As an atom approaches the surface (curve b), a strong interaction making electron transfer and then occurs forming with a chemical bond on the surface at a distance of r_c. Moreover, the energy (ΔE_D) seems less chemisorption of molecules because it is needed largely energy for the dissociation into atoms. In practice, the adsorption occurs through physisorption followed by chemisorption, requiring the energy (ΔE_A) less than ΔE_D. The rate of chemisorption from the gas phase molecules can be expressed as

$$d\Gamma_{CHEM} / dt = k_{ads} P\left(\Gamma^0 - \Gamma\right) exp\left(-\Delta E_A / RT\right) - k_{des}\Gamma exp\left[-\left(\Delta H_{CHEM} + \Delta E_A\right) / RT\right] . \quad (2.14)$$

At steady state, the equilibrium coverage becomes

$$\Theta = \Gamma / \Gamma^0 = k_{ads} / k_{des} exp\left(\Delta H_{CHEM} / RT\right). \quad (2.15)$$

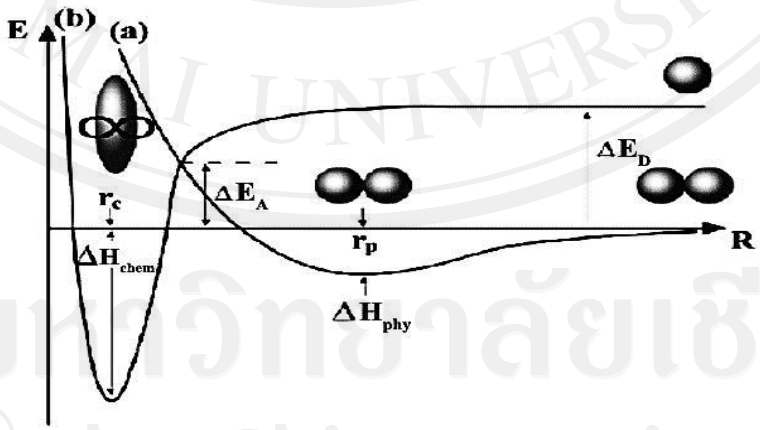

Figure 2.10 Lennard-Jones model for physical and chemical adsorption as a function of the energy of the system, and adsorbate/adsorbent distance: (a) physical adsorption and (b) chemical adsorption [123]

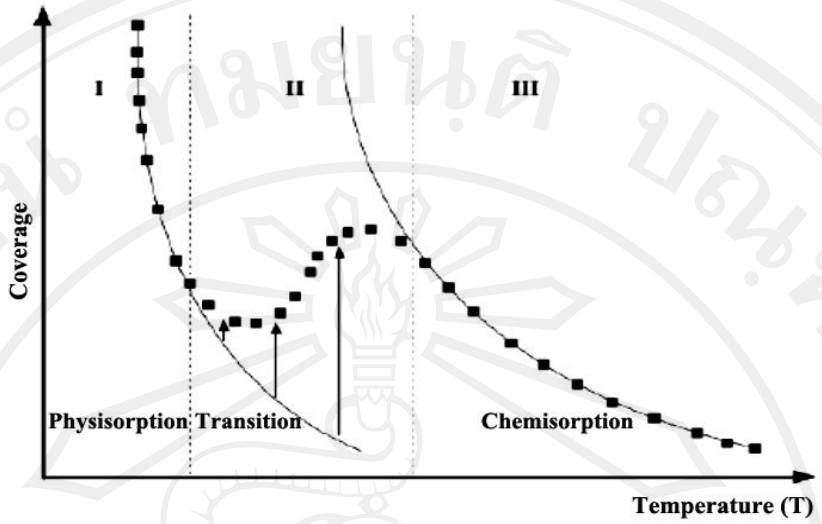

Figure 2.11 Isobar of typical adsorption: (I) physisorption, (II) irreversible transition and (III) chemisorption [123]

At elevated temperature, the adsorption and desorption process still requires energies compared with physisorption. Following the experimental, the activation energy, ΔE_A, increases according to increasing coverage at a given temperature, as shown in Figure 2.11. According to the Lennard-Jones model (Figure 2.10), the curve (b) will shift up as chemisorption progresses, while curve (a) remains unaffected. In Figure 2.11, the typical adsorption isobar, the coverage as a function of temperature at a constant gas pressure, is sketched as a dotted curve. At low temperature (region I), adsorption follows an inactivated physisorption process of curve (a) corresponding to Equation 2.13 and at high temperature (region III), equilibrium chemisorption occurs according to curve (b) in Equation 2.15. In the intermediate temperature range (region II), there is the transition from physisorption to chemisorption occurring such that physisorption at equilibrium is readily reached. By the way, the temperature (thermal energy) increases till overcome an activation barrier ΔE_A to provide more coverage

with temperature. Hence, coverage increases as temperature in region II where the theoretical desorption rate (the second term in Equation 2.14) is substantially lower than the adsorption rate until the equilibrium coverage in region III is reached (desorption rate becomes balanced with the adsorption rate, it corresponds with curve (b) in Figure 2.10).

To remove the adsorbate, the temperature has to be raised in region III, where the desorption rate becomes appreciable. This is a way for thermal cleaning at high temperature that is frequently performed to refresh the sensor. Thus, adsorption in the intermediate region is sometimes called “irreversible chemisorption” which the coverage depends on the properties of material from preparation method.

2.4.1.2 Surface states [123, 126]

The surface state is a localized electronic energy level at the surface. In ionic crystals such as semiconducting metal oxides, surface states can be classified into two kinds depending on the source: (1) intrinsic surface states resulting from the distortion of lattice periodicity at the surface only and (2) extrinsic surface states originated from the adsorption of gases or impurities on the surface. Tamm states used suitably for an ionic crystal appear whenever there is a large difference of the electron affinity between the surface species and the bulk species. Following Tamm states, surface cations will provide acceptor-like surface states (electron traps) near the conduction band while surface anions will provide donor-like surface states (hole traps) near the valence band. The classic Madelung model for ionic crystal can be used for explaining this as shown in Figure 2.12.

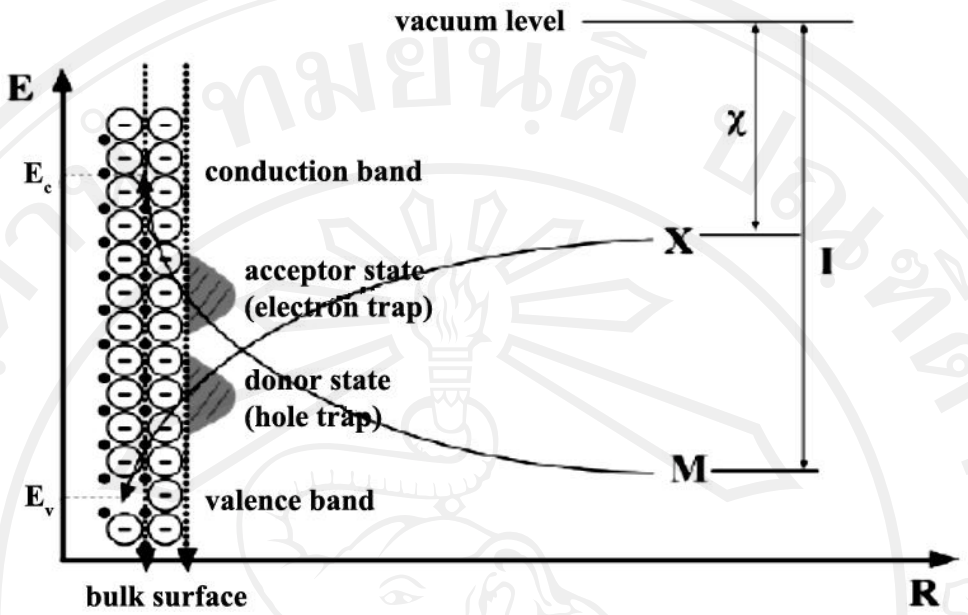

Figure 2.12 Madelung model of ionic solid MX; χ is the electron affinity and I is the ionization potential [123].

In Figure 2.12, the electron energy levels at the surface sites differ from those in the bulk, which produces the intrinsic surface states. The unoccupied orbital over the cation acts as an acceptor-like surface state (Lewis acid site) and the occupied orbital over the anion as a donor-like state (Lewis base site). For a covalent material, the atoms at the surface form dangling bonds, and an intrinsic surface state is called Shockley state.

When foreign atoms adsorbed on a new surface, it can inject into or capture electrons from the bulk to form a localized electron energy state at the surface (the so-called extrinsic surface state). Free species from this are modified by the Madelung potential of the lattice. In the presence of extrinsic or intrinsic surface states, electrons flow due to the difference in the energy levels of the surface state and the Fermi level (average energy of electrons) of the bulk. If surface state level of foreign atoms is

lower than the Fermi level in the bulk, it will capture electrons from the conduction band to form a depletion layer around the surface for n-type semiconductors and from the valence band to form a cumulative layer for p-type semiconductors. The former is called “depletive adsorption” due to the limited source of electrons in the conduction band and the latter “cumulative adsorption” due to the rich electrons existing in the valence band.

For instance, the adsorption of oxygen either molecule or atom on an ionic crystal can happen. The transfer of electrons from the bulk to the adsorbed oxygen due to the fact that the electron energy level of oxygen adsorbate becomes lower than that of the Fermi level in the ionic crystal following the process:

$$O_2 + e^- = O_2^- \tag{2.16}$$

$$O + e^- = O^- . \tag{2.17}$$

These charged particles are bonded to the surface via electrostatic forces, which is sometimes called “ionosorption,” a form of chemisorption. As the occupancy of the electrons in the surface states also has to relate with the Fermi statistics, the relative concentrations of O_2^- and O^- to O_2 and O can be written as

$$\left[O_2^-\right] / \left[O_2\right] = exp\left[-\left(E_{O_2^-} - E_F\right) / kT\right] \tag{2.18}$$

$$\left[O^-\right] / \left[O\right] = exp\left[-\left(E_{O^-} - E_F\right) / kT\right] \tag{2.19}$$

where $E_{O_2^-}$ and E_{O^-} are the surface energy levels for oxygen molecules and atoms, respectively. Additionally, oxygen molecules can dissociate into atoms on the surface of the oxide with the chemical reaction:

$$O_2 = 2O\,. \tag{2.20}$$

From Equations 2.16−2.20, the relative concentrations of O_2^- to O^- can be expressed as

$$\left[O_2^-\right]/\left[O^-\right] = \left[O_2\right]^{1/2} exp\left[-\left(E_{O_2^-} - E_{O^-} - 1/2\Delta G^O_{(2.22)}\right)/kT\right] \tag{2.21}$$

where $\Delta G^O_{(2.22)}$ corresponds to the standard Gibbs energy change for reaction (2.22). As a result of the large positive value of $\Delta G^O_{(2.22)}$, the concentration of O^- increases with increasing temperature, but decreases with increasing oxygen partial pressure.

2.4.1.3 Sensing mechanism [123−125, 127]

The presence of the negative charge on the n-type semiconductor metal oxide surface and of foreign atom absorbing on that surface leads to band bending (Figure 2.13). This would generate a surface potential barrier $eV_{surface}$ of 0.5 to 1.0 eV. The surface charge can indicate by the amount and type of absorbed oxygen. This is affect the height ($eV_{surface}$) and depth ($\wedge_{air}$) of the band bending. About the donor concentration of semiconductor metal oxide, the relationship between $\wedge_{air}$ and the Debye length L_D is showed as

$$L_D = \sqrt{\frac{\varepsilon_0 \varepsilon k_B T}{e^2 n_d}} \tag{2.22}$$

where k_B is Boltzmann's constant, ε is the dielectric constant, ε_0 is the permittivity of free space, T is the operating temperature, e is the electron charge, and n_d is the donor concentration for full ionizing.

This situation describes the idealized case where humidity is not involved in the surface chemistry. However, some real system under ambient conditions is under the influence of water-forming hydroxyl groups, which may affect the sensor performance.

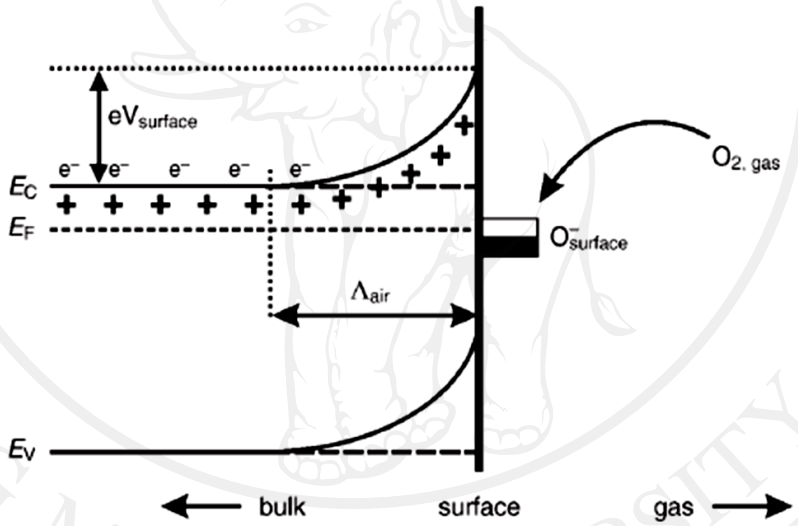

Figure 2.13 Schematic diagram model on band bending of wide bandgap semiconductor metal oxides after ionosorption of oxygen on surface sites. E_C, E_V and E_F are the energy of the conduction band, valence band, and the Fermi level, respectively, while $\wedge_{air}$ is the thickness of the space-charge layer, and $eV_{surface}$ is the potential barrier. The conducting electrons are represented by e^- and the donor sites are also represented by + [124].

Materials in the intergranular contact type, consisting of the space charge layer of electrons is usually more resistive than the bulk type. For total conductance of a porous medium, it is determined by the percolation path through the structural inhomogeneities over bulk grain and intergranular contacts. For the conduction of the intergranular contacts, electrons must overcome barrier in order to cross from one grain to another. In this case, the sensor conductance G can be written as

$$\mathrm{G} = \mathrm{G}_0 exp\left(-\frac{eV_{Surface}}{k_B T}\right). \tag{2.23}$$

The barrier height is proportional to the square of the coverage as shown in Equation 2.24:

$$eV_{Surface} = e^2 N_S^2 / 2\varepsilon_S N_i \tag{2.24}$$

where N_i corresponds to the net impurity concentration in the bulk, ε_S is the permittivity of the semiconductor and N_S is the surface state density. Furthermore, the conductivity has an exponential dependence to the square of the coverage when represent Equation 2.24 to 2.23.

According to Bârsan and Weimar, a power-law dependence of the conductance on the partial pressure of gas $\left[p_{\mathrm{gas}}\right]$ is given as $\mathrm{G} = [p_{gas}]^n$, where n depends on the morphology of the sensing layer and on the actual bulk properties of the sensing material.

Generally, the intergranular contacts can be classified into three cases, which give different dependences for conductance on the partial pressures of oxygen and combustible gases:

1. Bulk-trap-limited conduction process (Open Neck)
2. Surface-trap-limited conduction process (Closed Neck)
3. Schottky barrier-limited conduction process (Schottky Contact)

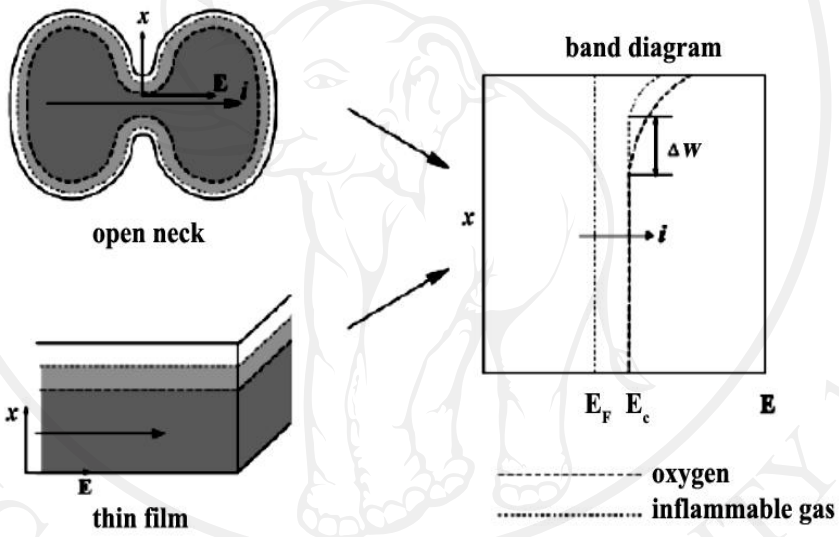

Figure 2.14 Schematic band structure and conduction process for a well-sintered ceramic and thin film gas sensor [123]

If the neck width L_D, the conductivity depends on the width of the undepleted layer and the rate of activation of electrons from the Fermi level in the bulk to the conduction band edge (bulk trap- limited conduction) expressed as

$$G \propto w exp\left[-\left(E_C - E_F\right)_b / k_B T\right] \qquad (2.25)$$

where w, E_C and E_F correspond to the depleted layer width, the conduction band edge and the Fermi level of the bulk oxide. In this case, the sensitivity toward the gas concentration can only be achieved by the variation of the effective width of the surface space charge layer (w) in Equation 2.25. These activities can be well found in a full sintered ceramic pellet with "open necks" or in compact and thin film structure with thickness much larger than L_D, as shown in Figure 2.14.

On the other hand, when the conduction width $\leq 2L_D$, the space charge layers from the other surfaces overlap to form a higher-resistance ohmic path through the depleted zone as shown in Figure 2.15. This is often found in a less sintered ceramic with "closed necks" or in thin films or pressed nano-crystalline ceramics. In this case, flat-band conditions are represented for understanding and the conductance is determined by the activation of electrons from the surface states to the conduction band edge at the surface (surface-trap-limited conduction) expressed as

$$G \propto exp\left[-\left(E_C - E_S\right)_S / k_B T\right] \tag{2.26}$$

where $\left(E_C - E_S\right)_S$ corresponds to the difference between the conduction band edge at the surface and the surface state energy level. The sensitivity is directly attained to the variation of the surface conduction band energy due to the direct change in the occupancy of surface states. This is similar to Rothschild and Komem model [128] which calculates the effective carrier concentration as a function of the surface state density. Therefore, a steep increase of the sensitivity is accordance with a critical value of the surface state density, or fully depleted grain. The critical value is proportional to grain size.

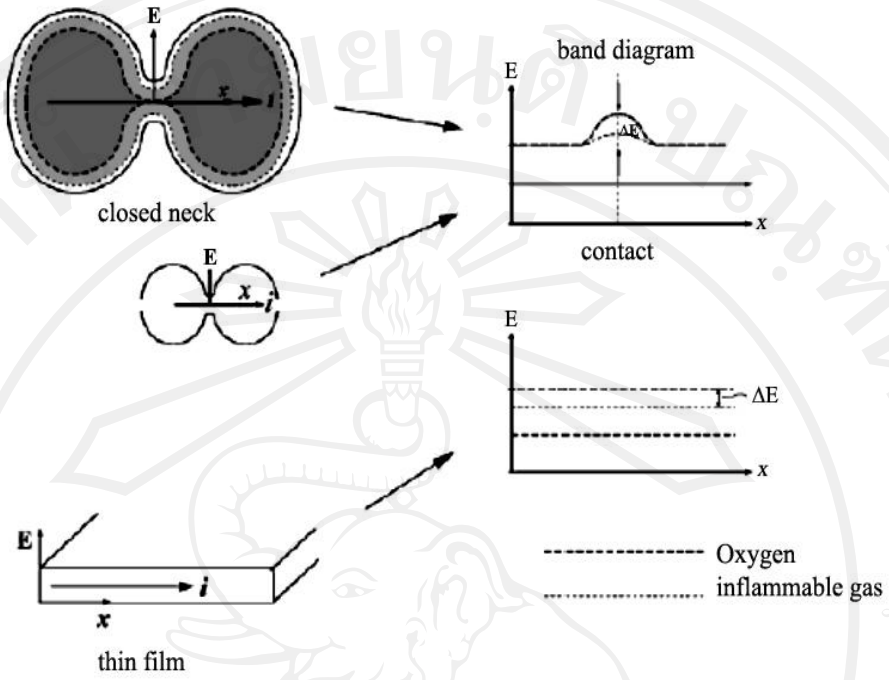

Figure 2.15 Schematic band structures for a less sintered ceramic, nanocrystallite or very thin film gas sensor with and without inflammable gas [123]

When the diameter of ceramic particles $\geq 2L_D$ are "pressed" together as shown in Figure 2.16, Schottky barrier-limited conduction with the surface barrier height, as shown in Equation 2.23. The conductance is limited by the electron transport across the barrier at the intergranular contact, which can be written as

$$G \propto exp\left[-eV_S / k_B T\right]. \tag{2.27}$$

Here, eV_S is the surface barrier height, which is directly proportional to the square of the occupancy of the surface states as in Equation 2.23. Hence, the resistance response of the sample becomes a sensitive function of the concentration of the gases in the ambient temperature as mentioned earlier.

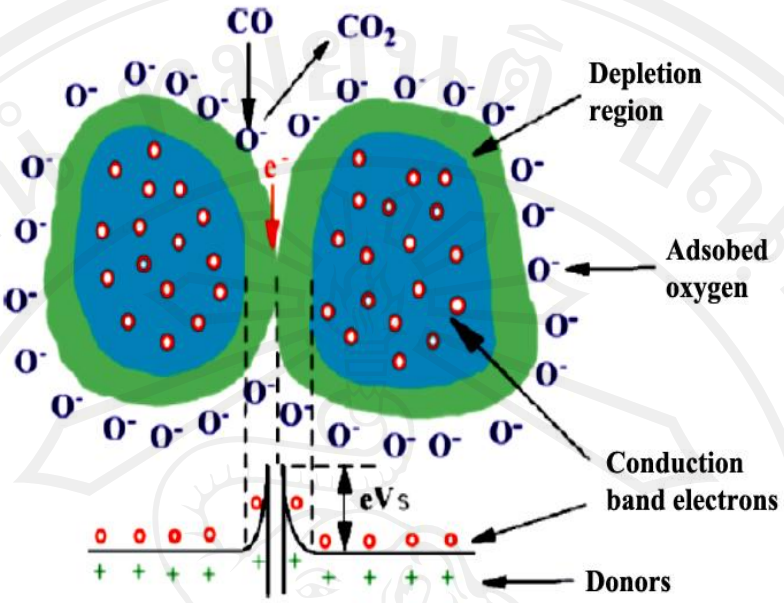

Figure 2.16 Schematic intergranular contacts for CO sensing in an n-type oxide [123]

2.4.2 DC resistance transduction [126]

DC resistance measurement is the easiest transduction for physical quantity on gas sensing. In laboratory test, it is normally measured by a voltamperometric technique at constant bias. However, in commercial gas sensors, the layer is inserted inside a voltage divider. In general, the response of semiconductor metal oxide sensors toward a target gas concentration (S_G) is defined as the relative change of conductance at absorption steady states of gas target (G_S) and oxygen (G_O) as follows:

$$S_G = \frac{G_S}{G_O} = \frac{G_S - G_O}{G_O} + 1 = S_G^* + 1. \qquad (2.28)$$

In case of an oxidizing target species, the resistance increases relating to gas introduction; the sensor response (S_R) is defined as the relative change of resistance at absorption steady states of gas target (R_S) and oxygen (R_O) as follows:

$$S_R = R_S / R_O = (R_S - R_O) / R_O + 1 = S_R^* + 1. \quad (2.29)$$

From the sensor response, it is possible to derive the sensor response curve, which is the representation of the steady state output as a function of the input concentration. The sensor response curve is often called erroneously to sensitivity curve.

2.5 Metal oxide for photocatalyst [66, 94, 129, 130]

2.5.1 Mechanism of metal-oxide-assisted photocatalytic degradation [94, 129, 130]

ZnO has a similar bandgap to that of TiO_2 and is expected to exhibit photocatalytic ability similar to TiO_2. This is provided that this property may get into the energy level of CB and VB. Therefore, it has been comparatively studied with TiO_2 in terms of its photocatalytic performance. The photomineralization with the breakdown of organic compounds carried out in aerated solution, which can easily summarize by the reaction:

$$Oraganic\,compound \xrightarrow{TiO_2,\, h\nu \geq E_g} CO_2 + H_2O + mineral\,acid\,. \quad (2.30)$$

A schematic representation of the photocatalytic activity is displayed in Figure 2.17. The photoexcitation with light energy, which is greater than the bandgap energy,

promotes an electron from the valence band to the conduction band. This is cause to creation an electronic vacancy or "hole" (h^+) at the valence band edge (Figure 2.17, path 1). Also, in Table 2.3, it can show each process possibly for the photocatalytic degradation in chemical reaction form including the time used in each process.

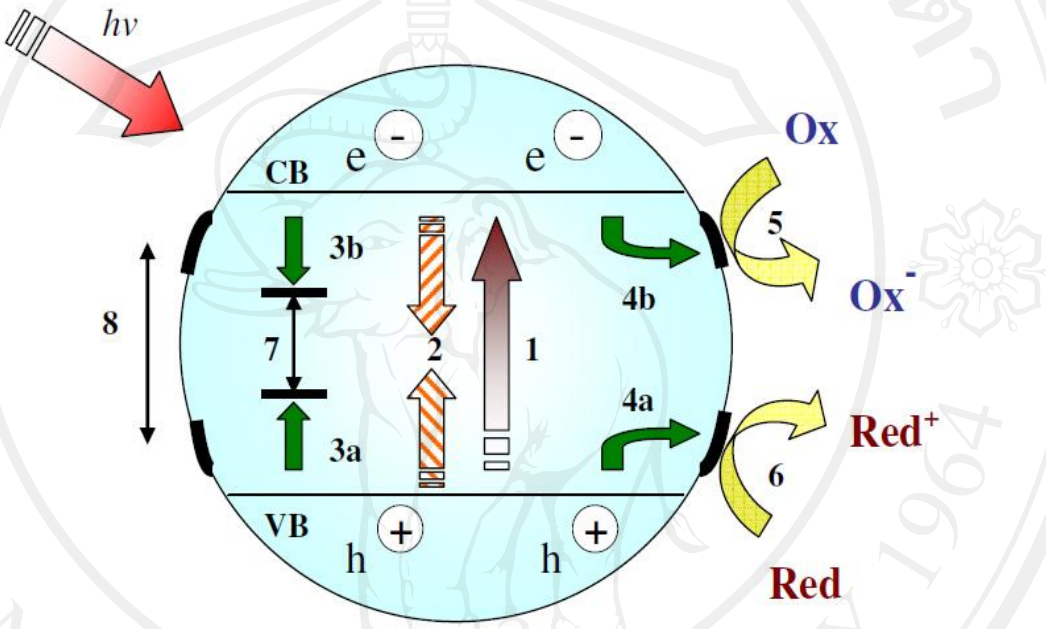

Figure 2.17 The multiple reaction processes of TiO_2 semiconductor under UV illumination: (1) electron excitation of semiconductor; (2) non-trapped exciton recombination; (3) deep trapping of (a) VB holes and (b) CB electrons; (4) shallow trapping of (a) holes and (b) electrons; (5) reductive foundation by shallowly trapped electrons; (6) oxidative foundation by shallowly trapped holes; (7) recombination of deeply trapped excitons and (8) recombination of shallowly trapped excitons [94]

Table 2.3 Primary processes and time estimation on TiO_2 photocatalytic activity process [94, 129]

Primary Process	**Characteristic Time**
(1) Bandgap excitation $TiO_2 + h\nu \rightarrow e^- + h^+$	Very fast
(2) Recombination of non-trapped excitons $h^+_{vb} + e^-_{cb} \rightarrow heat$	1 ns
(3) Charge-carrier deep trapping a) $h^+_{vb} + trap(+) \rightarrow trap - h^+_{tr}$ b) $e^-_{cb} + trap(-) \rightarrow trap - e^-_{tr}$ $e^-_{cb} + Ti^{IV} \rightarrow Ti^{III}$ when $trap(-) = Ti^{III}$	- - 10 ns
(4) Charge-carrier shallow trapping a) $h^+_{vb} + trap(+) \rightarrow trap - h^+_{tr}$ $h^+_{vb} + Ti^{IV}OH \rightarrow Ti^{IV}OH^+$; when $trap(+) = Ti^{IV}OH$ b) $e^-_{cb} + trap(-) \rightarrow trap - e^-_{tr}$ $e^-_{cb} + Ti^{IV}OH \rightarrow Ti^{III}OH$; When $trap(-) = Ti^{III}OH$ Where $Ti^{IV}OH$ is the surface titanol moiety	- 10 ns - 100 ps

Primary Process	Characteristic Time
(5) Interfacial charge transfer $trap - h_{tr}^{+} + Red \rightarrow trap(+) + Red^{+}$ Where Red is electron donors	100 ns (slow)
(6) Interfacial charge transfer $trap - e_{tr}^{-} + Ox \rightarrow trap(-) + Ox^{-}$ where Ox is scavenging species	ms (very slow)
(7), (8) Recombination of deeply/shallowly trapped charge carriers $trap - h_{tr}^{+} + trap - e_{tr}^{-} \rightarrow trap(+) + trap(-)$ $e_{cb/tr}^{-} + trap - h_{tr}^{+} \rightarrow trap(+)$ $h_{vb/tr}^{+} + trap - e_{tr}^{-} \rightarrow trap(-)$	- 100 ns (slow) 10 ns (fast)

The process of charge formation is very rapid and was reported in the order of femtoseconds (fs). Under exciting, approximately 90% of the exciton pairs may really recombine within 1 ns. For the remaining exciton pairs, they are captured either at deep (lattice) traps or, at shallow (surface) traps (in the case of their diffusion far enough). The spent time for shallow trapping of holes and electrons, is expected to be in the order of 10 ns and 100 ps, respectively. In other words, deep trapping of electrons is required around 10 ns. This trap of excitons can be mentioned that it is because of interstitial atoms, impurities, dislocations or even defects.

In the case of shallow trapping of electrons at Ti^{IV} sites is denoted as trap (+) to form Ti^{III} and that of hole trapping at surface $Ti^{IV}OH$ is recognized that $Ti^{IV}OH^{\bullet+}$ (surface bound hydroxyl radicals) are result. This reversible shallow trapping of electrons exists in dynamic equilibrium at room temperature so there is sufficient energy for the trapped electrons, e_{tr}^{-}, to be transferred back to the CB. Unlike shallowly trapped holes regarded as a very high potential oxidative reactant, deeply trapped holes are long-lived and unreactive. For the trapped electrons and holes (Figure 2.17, paths 3 and 4), it can be explained that the energy potentials of these electrons and holes drop below that of normal CB and VB.

The interfacial charge transfer is believed to be the most difficult path in typical photocatalytic reaction since its process time so long (about 100 ns to even ms). Moreover, absolutely, there is concurrently the recombination of trapped charge carriers. The appearance of photocatalytic reaction is regularly referred to the surface redox exchange. The nanoparticles of n-type semiconductor are unlike the bulk of that on photocatalytic activity, for the reason that the nanoparticles can simultaneously present both photo-oxidation and -reduction reaction on their surface while the bulk is still on only photo-oxidation reaction due to band bending.

The average transit time of the photogenerated charges, τ_{tr}, within a particle with its diameter, D_a, can be obtained by solving Fick's diffusion law:

$$\tau_{tr} = \frac{D_a{}^2}{4\pi^2 D} \tag{2.31}$$

in which D is the diffusion coefficient. Hence, it can imply that the photocatalytic efficiency is upon a competition between the recombination of trapped carriers and interfacial charge transfer.

The efficient scavenging species (Ox) generated from dissolving of O_2 is essential for any photocatalytic studies. The energy potential of O_2 molecule over reduction reaction is almost equivalent with CB potential of the metal oxide catalysts. In fact, the electron scavenging by O_2 is so efficient that it has to be removed during photoreduction of metal cations or water splitting for H_2 generation. From attacking other organic molecules on photocatalysis, the resulting superoxide radical $O_2^{\bullet-}$ is capable or in some cases could function as an alternative source of surface bound hydroxyl radicals upon protonation. In case of the absence of O_2 (anoxic) in the system, highly electronegative inorganic species such as Fe^{3+}, Ag^{+}, $PtCl_6^{2-}$, $AuCl_4^{2-}$, $S_2O_8^{2-}$ or even organic species such as hydroquinone, methyl viologen, chlorinated compounds, could be used as the sacrificial electron scavenging agent (Ox).

For generating hydroxyl radical $OH^{\bullet}$, it can be possible in two ways: holes trapping at surface $Ti^{IV}OH$ from absorbing water at surface of catalysts, giving the surface bound hydroxyl radical species or direct holes transferring to the water molecule (Red) through the rapid fragmentation of $H-OH^{\bullet+}$, giving non-surface bound hydroxyl radical species. Such free (non-surface bounded) $OH^{\bullet}$ can diffuse to the bulk solution. In this case, it would attack poorly adsorbed organic species. However, both surfaces bound and free $OH^{\bullet}$ are commonly high oxidizing power. Their energy potentials over oxidation reaction are only slightly lower that of VB.

Moreover, the oxidation of organic species could occur possibly through $OH^{\bullet}$ or directly by h_{tr}^{+}.

In addition, the formation of H_2O_2 is possible due to the redox potential of the electron-hole pair, either through water oxidation (by holes) or by two conduction band electron reduction of the adsorbed oxygen, as shown in Figure 2.18. H_2O_2 correlates with the degradation process by acting as an electron acceptor or as a direct source of hydroxyl radicals due to homolytic scission. Under the photocatalytic reaction, the holes, $OH^{\bullet}$ radicals, H_2O_2 and O_2 can be a part of this mechanism, also depending on the reaction conditions. For all possibilities of the photooxidative degradation processes, they are presented in Figure 2.18.

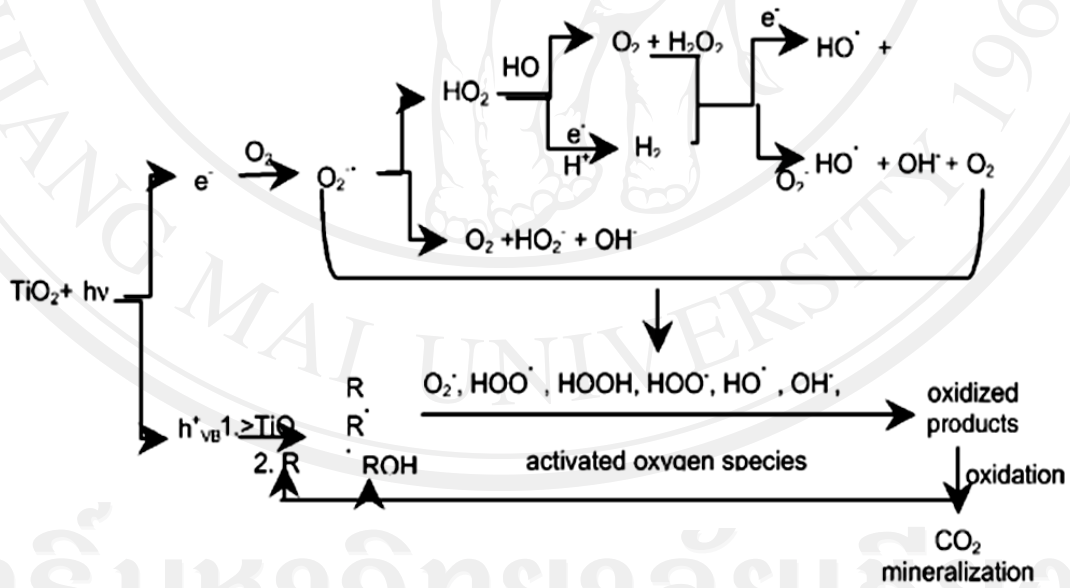

Figure 2.18 The several possible reactions with activated oxygen in the mechanism of photooxidative mineralization of organic compounds [129]

In the case of ZnO the rather limited property of ZnO particles in an aqueous environment is its chemical instability because of its photo-corrosion with UV irradiation as follows:

$$ZnO + 2H^{+}_{ad} \rightarrow Zn^{2+}_{aq} + H_2O \quad (2.32)$$

$$ZnO + H_2O \rightarrow Zn(OH)_2 . \quad (2.33)$$

The release of Zn^{2+} ions in solution and the formation of $Zn(OH)_2$ at the surface, significantly reductions the photocatalytic activity of ZnO and also blocks its applied application in environment purification. Moreover, the pH range with using ZnO is found to be stable and very limited. The oxidation pathways of ZnO are similar to those of TiO_2, including the formation of $OH^{\bullet}$ radicals as well as the direct oxidation by photogenerated holes, etc. Furthermore, under prolonged optical irradiation, ZnO undergoes the self-photodecomposition. The oxidation of ZnO from the solid phase into the aqueous phase by holes corresponds to the following reaction:

$$Zn + 2h^{+}_{VB} \rightarrow Zn^{2+} + \tfrac{1}{2} O_2 . \quad (2.34)$$

However, the advantages of ZnO application were reported about an absorption capacity which is larger fractions of solar spectrum, compared to TiO_2 [131]. In addition, the typical electron mobility in ZnO is 10–100-fold which is higher than that in TiO_2, leading to reduce electrical resistance and enhance electron transfer efficiency [132]. Fortunately, for these reasons, ZnO in nanoscale is considered to be a suitable photocatalyst for catalytic removal of pollutants in the presence of sunlight.

Recently, the various methods have been developed to quench the photogenerated electrons to reduce the extent of photo-corrosion as well as suppress the undesired charge carrier recombination of ZnO to enhance the activity. Surface modification is an answer with either by doping with metals and non-metals or composite formation (coupling of two or more semiconductors), by mutual transferring of charge carriers from one semiconductor to the other, depending on their compatible chemical and electrical properties [133].

2.5.2 Langmuir-Hinshelwood kinetics [66]

The kinetics of photocatalytic degradation of organic compounds usually matches with the Langmulr-Hinshelwood model.

Table 2.4 Langmuir-Hinshelwood model assumptions [66]

Number	Explanation
1	The number of surface adsorption sites is fixed at equilibrium.
2	Only one substrate may bind at each surface site.
3	The heat of adsorption by the substrate is identical for each site and is independent of surface coverage.
4	There is no interaction between adjacent adsorbed molecules.
5	The rate of surface adsorption of the substrate is greater than the rate of any subsequent chemical reactions.
6	No irreversible blocking of active sites by binding to product occur.

The pre-adsorption of substrate on a photocatalyst can be explored by the use of a Langmuir-Hinshelwood (LH) kinetic model modified to fit reactions occurring at a solid-liquid interface. The model assumptions are indicated in Table 2.4. The surface coverage θ_S is related to the initial concentration of the substrate C and to the apparent adsorption equilibrium constant K_1 (Equation 2.35). The rate of product formation can then be written as a single-component LH kinetic rate expression (Equation 2.36)

$$\theta_S = KC / (1 + KC) \tag{2.35}$$

$$r_{LH} = -dC / dt = kKC / (1 + KC) \tag{2.36}$$

where k is the apparent reaction rate constant occurring at the active site on the photocatalyst surface. The linearity of a plot of l / r_{LH} versus $1 / C$ is confirmed according to the LH model, where $1 / k$ is the y intercept and $1 / kK$ is the slope. Many photocatalytic reactions show good linearity. Nevertheless, this fit cannot be taken as a solid proof of preadsorption since an identical analytical formulation of the rate law is obtained even for reactions occurring entirely within a homogeneous phase. The linearity reveals to the expectation of the photocatalytic decomposition that it occurs completely on the catalyst surface. Actually, this study indicated that the analytically identical rate expressions would be obtained if the reaction between substrate and photogenerated oxidant were to occur while both species were adsorbed, with an adsorbed substrate and a free oxidant, with a bound oxidant and a free substrate, or with both the oxidant and substrate freely dissolved. The processes on diffusing surface-generated catalytic species to the bulk solution are described by an

Eley-Rideal pathway. An experimental distinction between these pathways, based on kinetics alone, is not possible due to the kinetic ambiguities discussed above.

Moreover, the LH approach still possesses inherent limitation since it avoids a complex mathematical formulation of surface binding, and the need for several experimentally undeterminable parameters. In the case of two or more species which there is the competition between them for a single adsorption site, the suggested reactions to involve these are shown as follows:

$$r_{LH} = kKC / \left(1 + KC + \sum_i K_i C_i \right) \tag{2.37}$$

where i is a competitively adsorbed species.

Since a basic assumption of the LH kinetic model is the requirement for surface preadsorption, the large difference of reaction rates might reasonably be expected from varying the adsorptive affinity of different substrates on a semiconductor surface. However, the observed rates k are surprisingly similar in different reactions that have been studied.